Energy 166 (2019) 789–795

Contents lists available at ScienceDirect

Energy

journal homepage: www.elsevier.com/locate/energy

Innovative multipolymer electrolyte membrane designed by oxygen inhibited UV-crosslinking enables solid-state in plane integration of energy conversion and storage devices

Alberto Scalia [a, *], Federico Bella [b, **], Andrea Lamberti [a], Claudio Gerbaldi [b], Elena Tresso [a]

[a] Department of Applied Science and Technology - DISAT, Politecnico di Torino, Corso Duca degli Abruzzi 24, 10129 Torino, Italy
[b] GAME Lab, CH ENERGY Group, Department of Applied Science and Technology - DISAT, Politecnico di Torino, Corso Duca degli Abruzzi 24, 10129 Torino, Italy

ARTICLE INFO

Article history:
Received 7 March 2018
Received in revised form
21 September 2018
Accepted 27 October 2018
Available online 29 October 2018

Keywords:
Photocapacitor
Integrated solar capacitor
Multipolymer electrolyte
UV curing
Dye-sensitized solar cell
Electrochemical double layer capacitor

ABSTRACT

In this paper a novel polymer-based platform is applied for the fabrication of an innovative two-electrodes self-powered device integrating energy harvesting and storage sections. A multifunctional polymeric layer, made of two poly(ethylene glycol)-based sections separated by a perfluorinated barrier, is obtained by oxygen-inhibited UV-light crosslinking procedure. For the energy harvesting section, one side of the polymeric layer is adapted to enable iodide/triiodide diffusion in a dye-sensitized solar cell (DSSC), while the other side empowers sodium/chloride ions diffusion and is used for on-board charge storage in an electrochemical double layer capacitor (EDLC). The resulting photocapacitor has a planar architecture appreciably simplified with respect to other recently proposed solutions and more easily exploitable in low power electronics. The measured photo-electrical conversion and storage total efficiency is 3.72% during photo-charge, which is a remarkable value for DSSC-EDLC harvesting-storage devices literature. The obtained high frequency discharge capability enlightens promising prospects for practical applications in low power portable electronics.

1. Introduction

Electrical energy harvesting and storage (HS) devices have attracted sizeable attention in recent years due to the growing power demand in off-grid conditions requested by flexible and portable electronics or sensor networks [1,2]. This clearly drives towards enormous advancements in the development of innovative smart multifunctional materials for sensors [3,4], energy conversion [5–14] and storage devices [15–21]. In particular, the production of portable power supply units for actuation of low power electronics [22–24], biomedical microdevices [25,26] and sensing elements exploiting self-charging approach [27–30] is of great importance.

In this scenario, different architectures have been proposed, which enable to couple energy conversion (photovoltaic, piezoelectric and triboelectric) and storage (supercapacitors, batteries) technologies. Xue et al. [12] proposed an interesting monolithic hybridization of piezoelectric and battery units, where the former is used to convert mechanical energy into electricity, which can be stored in the form of chemical energy by the latter. Such an approach brings forward the production of self-charging power cells for sustainable driving micro/nanosystems and low power electronics. Wang et al. [22] described a flexible and wearable self-charging power system consisting of a fiber supercapacitor and a fiber-based triboelectric nanogenerator. It also describes the first prototype of wearable electronics assuring mechanical energy harvesting from human motion.

Photovoltaic (PV)-based HS devices have been thoroughly investigated in the last years, allowing to achieve really efficient (and even highly flexible) configurations [31–35]. In this context, photovoltaic-supercapacitor integration would represent a concrete strategy towards the development of commercial HS devices if a couple of requirements were met: i) the selection of a suitable PV-harvester; ii) the development of high performing materials being also economic and industrially scalable. At present, dye-sensitized solar cells (DSSCs) represent the best choice in terms

* Corresponding author.
** Corresponding author.
E-mail addresses: alberto.scalia@polito.it (A. Scalia), federico.bella@polito.it (F. Bella).

https://doi.org/10.1016/j.energy.2018.10.162
0360-5442/

of performance, versatility [36–38] (flexible designs, indoor efficiency) and overall cost [39,40]. As for the electrolyte materials, polymers can represent a successful choice, not only for their intrinsic characteristics, but also under the industrial viewpoint as they can be manufactured by high-speed technologies (such as UV or thermally induced radical polymerization), which also accounts for energy saving and low cost [41,42]. Finally yet importantly, literature reports about PV-based HS devices deal with three or even four electrodes architectures, strongly affecting the complexity of device fabrication and integration processes [1,31,43].

In this work, we propose the first example of two electrodes HS device, which makes use of a multifunctional polymer electrolyte to successfully integrate a dye-sensitized solar cell and an electrical double layer capacitor in an appreciably simplified and fashionable way if compared to common architectures. The newly developed polymer electrolyte membrane consists of two poly(ethylene glycol)-based sections separated by a perfluorinated barrier, and it is prepared by UV-induced photopolymerization exploiting the inhibitory effect of oxygen during UV irradiation under air (oxygen-inhibited UV-curing, OI-UVC). One side is adapted to enable iodide/triiodide diffusion in the DSSC, and the other side empowers the functioning of the EDLC, which allows to exploit the same electrode for the two harvesting and storage units, thus strongly simplifying the overall device architecture (see Fig. 1). To our knowledge, such a peculiar device assembly has never been reported so far in the literature, due to the intrinsic issue of developing a single layer polymer electrolyte membrane that can assure concurrent operation of the EDLC and the DSSC units in a planar configuration. Here, an organic solvent-based electrolyte for the harvesting unit and an aqueous-based electrolyte for the storage unit effectively coexist in a smart architecture, thanks to the presence of an impermeable perfluorinated barrier layer. The obtained integrated device shows impressive HS combined performance. The overall photon-to-electrical conversion and storage efficiency (OPECSE) reached a maximum of 3.72%, also providing a remarkable discharge capacity of 20 mC cm^{-2} at 3 mA imposed discharge current, which is higher compared to most of the DSSC-EDLC HS devices reported so far in the literature [33,43–45], and definitely remarkable being the sole example of two electrodes quasi-solid integrated system.

2. Experimental section

2.1. Materials

Bisphenol A ethoxylate dimethacrylate (BEMA, average Mn: 1700), poly(ethylene glycol) methyl ether methacrylate (PEGMA, average Mn: 500), sodium iodide (NaI), iodine (I_2), 4-*tert*-butylpyridine (TBP), acetonitrile (ACN) and ethanol were purchased from Sigma-Aldrich.

2-hydroxy-2-methyl-1-phenyl-1-propanone (Darocur®1173) from Ciba Specialty Chemicals was used as free radical photoinitiator for crosslinking both the fluorinated separator and the methacrylic-based polymer sections of the multifunctional polymer electrolyte. Titanium metal grids were provided by Dexmet Corporation. TiO_2 paste (18NR-AO, active opaque titania paste) was purchased from Dyesol. N719 (Ruthenizer535bis-TBA) was purchased by Solaronix.

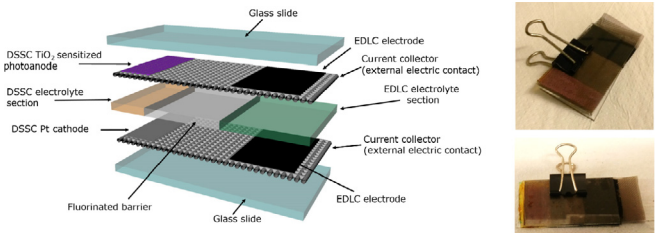

Fig. 1. 3D representation and pictures of the integrated HS device, showing the different components and the smart multifunctional polymer electrolyte membrane.

2.2. Preparation of the electrodes

Ti metal grids were cut into a 6 cm × 2.5 cm rectangular shape (see Fig. 1). Before use, they were cleaned in an ultrasonic bath in acetone for 10 min step, followed by 10 min rinsing in ethanol, and finally dried onto a hot plate at 100 °C under nitrogen flow to ensure the complete removal of solvent traces.

The DSSC electrode, which is directly exposed to light during operation, was obtained by doctor blading a uniform and homogeneous mesoporous TiO_2 layer (80 μm, 18NR-AO paste) onto one side of the metal grids (1 cm × 2.5 cm active surface, left hand side of Fig. 1), which was then sintered at 515 °C for 30 min. Photoelectrode was activated by deep soaking into a 0.3 mM N719 dye solution in ethanol for 12 h at ambient temperature, and then rinsed in ethanol to remove the unadsorbed dye molecules. The counter electrode (DSSC Pt cathode, same area as the photoanode) was obtained by sputtering (Q150T ES, Quorum Technologies Ltd.) a very thin (5 nm) layer of platinum onto the rear Ti grid (see Fig. 1) using a mask to avoid any contamination of the EDLC-side electrode.

The composite active electrode material of the EDLC was based on activated carbon (Norit SA SUPER), mixed with 5% of poly(-vinylidene fluoride) (PVDF, Solvay Solef® 6020) in excess of dimethyl sulfoxide (DMSO) as binder. The obtained slurry was doctor-bladed in the form of a uniform film (80 nm thick) onto both the Ti grids (2 cm × 2.5 cm active area of the electrodes, right hand side, see Fig. 1). After a rest time of 3 h to obtain a uniform deposition, the electrodes were dried onto a hot plate at 100 °C to ensure the evaporation of residual DMSO. The electric contact was placed on the EDLC section, on the far right hand side of the Ti grid (1 cm × 2.5 cm area, see Fig. 1), to measure the photo-changing voltage.

2.3. Preparation of the multifunctional polymer electrolyte membrane

The multifunctional polymer membrane was prepared by oxygen-inhibited UV-curing (OI-UVC). A liquid reactive mixture of perfluoropolyether Fluorolink® MD700 monomer and Darocur® 1173 free-radical photoinitiator (3 wt%) was casted onto the rear Ti grid, covering an active area of 2 cm × 2.5 cm between the DSSC and EDLC electrodes, and sandwiched between two transparent glasses separated by 100-μm thick Parafilm® tapes. The sandwiched blend was UV irradiated for 2 min (irradiation intensity on the sample surface of 30 mW cm^{-2}) under a medium vapour pressure Hg lamp (Helios Italquartz, Italy) in air atmosphere. The oxygen atmosphere inhibits surface crosslinking, thus leaving a thin layer of uncured liquid reactive monomer mixture on the external sides and edges of the fluorinated polymer separating section. After removal of the Parafilm® tapes, the methacrylic (pre) polymer mixture was casted (and contacted) left and right of the fluorinated polymer section (2 cm × 2.5 cm for the EDLC section and 1 cm × 2.5 cm for the DSSC section), again between the two transparent glasses separated by 100-μm thick Parafilm® tapes on the borders. The liquid reactive (pre)polymer mixture was made of bisphenol A ethoxylate dimethacrylate (BEMA), a methacrylic monomer having a double functionality, and poly(ethylene glycol) methyl ether methacrylate (PEGMA), a monofunctional

methacrylate, in the 35 to 65 ratio; 3 wt% of Darocur 1173 was added as photoinitiator. The mixture was UV irradiated for 2 min under flowing nitrogen to obtain a fully crosslinked multifunctional polymer network. It was contacted with the rear electrode (comprising the platinised counter electrode of the DSSC and the carbon-based EDLC electrode) laying onto a transparent glass. The two polymer film sections spaced by the fluorinated buffer were separately swelled dropwise by different liquid electrolyte solutions: 0.45 M sodium iodide, 0.056 M iodine and 0.55 M 4-*tert*-butylpyridine dissolved in acetonitrile and 2 M sodium chloride in water for the DSSC and the EDLC sections, respectively.

The final lab-scale quasi-solid HS device assembly was obtained by contacting the Ti metal grid supported front electrode (comprising the sensitized TiO_2 DSSC photoanode and the carbon-based EDLC electrode), laying on the upper transparent glass, with the obtained multifunctional quasi-solid polymer electrolyte. Common clips were used to consolidate the final assembly and guarantee a homogeneous and uniform assembly of the different components, thus assuring proper operation of the whole device during photocharge and subsequent discharge.

2.4. Characterization of the multifunctional polymer membrane and lab-scale quasi-solid HS device

FT-IR transmittance spectra of the multifunctional polymer membrane were collected on a Tensor 27 FTIR Spectrometer (Bruker). The averaged signal was collected with a resolution of 2 cm^{-1} from 4000 to 400 cm^{-1}.

Contact angle measurements were performed using OCA H200 Dataphysics equipment in ambient conditions. The sessile drop method was implemented employing blue aqueous solution as test liquid with 1.5 μL volume of the droplets.

The DSSC section performances were tested with a 91195 Newport solar simulator and a 2440 Keithley Source measure unit (SMU) in a 2 electrodes DSSC configuration having the same area (1 cm × 2.5 cm) of the DSSC section in the HS device. The solar simulator provided a power radiation intensity of 100 mW cm^{-2} with an AM1.5G spectrum, while the SMU applied a changing bias potential to the cell and acquired a current value for every applied potential. Cyclic voltammetry of the EDLC section was performed in 2-electrodes configuration, having the same area (2 cm × 2.5 cm) of the storage section in the HS device, at different scan rates with a Metrohm Autolab PGSTAT128 potentiostat/galvanostat. Constant current (galvanostatic) charge/discharge (CCCD) measurements were performed on the SMU, which was also used to obtain the I-V profiles of the DSSC.

The integrated HS device was tested under the same illumination conditions used for DSSC characterization (100 mW cm^{-2} with an AM1.5G spectrum) upon photocharge and in dark conditions during discharge. The terminals of the SMU were connected to the right hand side of the photo-capacitor, where a free space was left for the electrical contact close to the ELDCs electrodes (see Fig. 1).

3. Results and discussion

3.1. Characterization of the multifunctional polymer membrane

The smart polymer membrane capable - at the same time - to act as ionic conductor and separator, was prepared by the OI-UVC technique. Even if it is well known that UV-curing is a rapid, solvent-free and cheap process to produce 3D-crosslinked polymeric matrices, it is interesting to point out that oxygen inhibition (a relevant drawback of radical photopolymerization processes) can be exploited to control the sample surface and design multipolymeric materials. In our case, a 100 μm-thick layer of the perfluoropolyether Fluorolink® MD700 monomer (containing two methacrylic reactive units) was casted onto a glass support and UV-cured under ambient air. The presence of oxygen inhibited surface curing of the fluorinated monomer, which resulted in the crosslinking of the bulk of the sample to form of a solid crosslinked inner network, while a layer of uncured liquid monomer remained on the external side [46,47]. Immediately after, a liquid reactive mixture of two ethoxylated monomers (BEMA and PEGMA, as detailed in the Experimental section) was casted on the left and right sides of the fluorinated unit, and cross-linked by UV-light under controlled nitrogen atmosphere. The overall procedure (less than 3 min) is sketched in Fig. 2A. It allowed the concurrent crosslinking of the BEMA/PEGMA mixture to form a solid polymer network, and the crosslinking between the BEMA/PEGMA mixture and the fluorinated matrix by exploiting the layer of uncured liquid monomer still present on the external sides of the latter, resulting in a uniform multifunctional polymer platform. A picture of the multipolymer membrane before swelling in liquid electrolytes is shown in Fig. 2B.

The proper separation between the ethoxylated lateral units (blue spectra) and the fluorinated spacer (red spectrum) was evaluated by attenuated total reflectance Fourier transform infrared (ATR-FTIR) spectroscopy and optical contact angle measurements and the results are shown in Fig. 2C, D and 2E. By means of ATR-FTIR analysis we were able to clearly distinguish the BEMA/PEGMA profile, where the main signals of the methylene groups (~2800 cm^{-1}) and of the carbonyl unit of the acrylic groups (1730 cm^{-1}) are observed, from the fluorinated one, where the characteristics C—F stretching is observed at 1074 and 1127 cm^{-1}. In both the ethoxylated and fluorinated sections, the characteristic signal of (meth)acrylic double bonds at 1640 cm^{-1} is absent, confirming the complete crosslinking upon UV-curing.

A blue aqueous solution was used as test liquid during contact angle measurements (see Fig. 2E), where a drop was dispensed exactly at the interface between the two different polymer matrices. As soon as the liquid got in contact with the

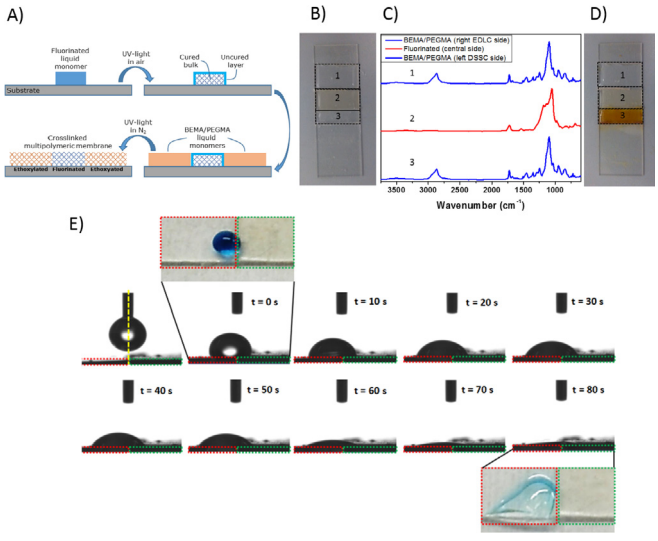

Fig. 2. A) Schematic illustration of the OI-UVC preparation process of the multifunctional polymer layer; B) Multipolymeric membrane before swelling; C) ATR-FTIR spectra of the three different sections of the multifunctional polymer membrane; D) Multipolymeric membrane swelled in the iodine-based liquid electrolyte (DSSC side) and NaCl aqueous electrolyte (EDLC side); E) Contact angle measurements test showing the time evolution of the blue drop onto the heterogeneous surface of the multifunctional polymer membrane (insets at t = 0 and 80 s show the characteristics of the drop in top views digital photographs).

heterogeneous surface (time t = 0 s, see inset photograph of the top view), it moved toward the most wettable side of the polymer film, i.e. the ethoxylated one. During the following 80 s, the liquid drop was fully soaked by the BEMA/PEGMA portion of the membrane being hydrophilic in nature. The fluorinated section remained fully uncoloured (as clearly evident in the inset photograph of the top view) at the end of the test, thus accounting for its excellent buffering ability to keep separated the two ethoxylated units when swollen by different liquid electrolytes.

The newly developed multifunctional polymer electrolyte membrane was assembled in a lab-scale quasi-solid HS prototype, as described in the Experimental section, and deeply characterised in terms of its electrochemical behaviour.

3.2. Characterization of the EDLC and of the DSSC

The storage section was firstly characterised by constant current galvanostatic charge discharge (CCCD) measurements. The corresponding profiles at different imposed constant currents are shown in Fig. 3A. The well-evidenced triangular shape accounts for remarkable electrical double layer capacitor characteristics. If compared to a previous work [31], the decrease of the thickness of the polymer electrolyte membrane (100 μm) led to a much higher Coulombic efficiency. This is likely ascribed to the lower average path that ionic species have to travel within the polymer matrix, thus resulting in a lower electrolyte bulk resistance. Indeed, a Coulombic efficiency value slightly lower than 95% was found only

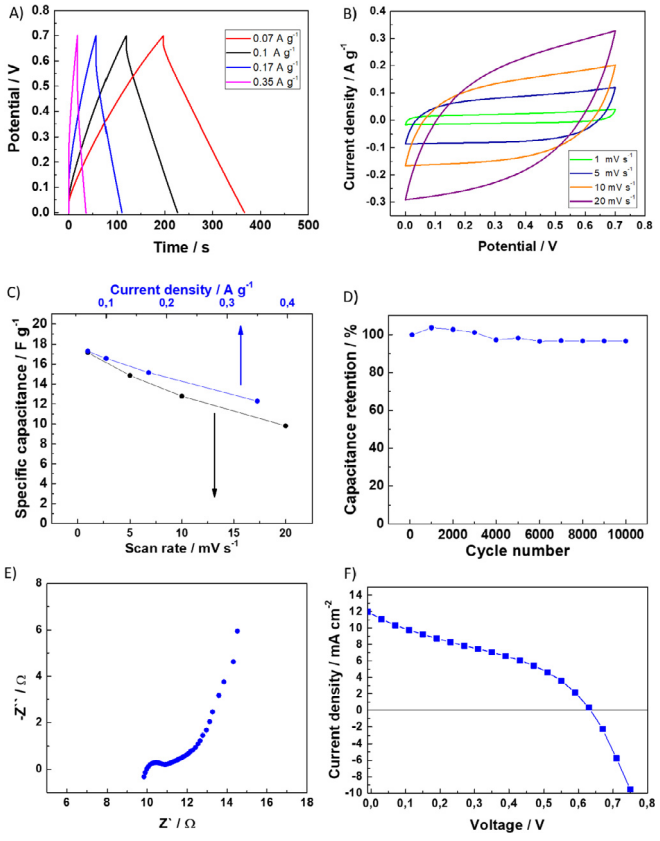

Fig. 3. Electrochemical characterization of the separate EDLC and DSSC sections of the integrated quasi-solid HS device. A) EDLC constant current charge discharge (CCCD) profiles at different current densities, B) EDLC cyclic voltammetry (CV) profiles at different scan rates, C) EDLC specific capacitance evaluated from CCCD plotted as a function of the current density and from CV plotted as a function of the scan rate, D) capacitance retention of the EDLC evaluated by repeated CVs, E) Nyquist plot of the EDLC, F) j-V measurement of the DSSC under 1 sun irradiation.

at the lowest current density applied. At higher current density values, the Coulombic efficiency increased well above 95%, finally approaching 99%, which is remarkable for a truly quasi-solid HS system. The device specific capacitances were evaluated from the discharge curves of the galvanostatic measurements, using the following equation [48]:

$$C = \frac{I\Delta t}{Vm} \tag{1}$$

where I is the constant current, Δt is the discharge time corresponding to the specific potential variation ΔV and m represents the weight of active material in the electrodes.

The cyclic voltammetry (CV) profiles at different scan rates for a 2-electrodes configuration are shown in Fig. 3B. An almost defined rectangular shape is obtained at low scan rates. Clearly, a resistive component due to the quasi-solid electrolyte affects the voltammetric response particularly at high scan rates. The capacitance values were evaluated from CV using the following equation [48]:

$$C = \frac{\int_0^{V/v} |i| dt}{Vm} \tag{2}$$

where V is the maximum potential reached during CV, v is the scan rate, i is the recorded current and m represents the weight of active material in the electrodes.

In Fig. 3C the specific capacitance values are plotted as a function of the constant current used in CCCD and as a function of the scan rate adopted during CV. An increased scan rate in the CV led to a slightly lower capacitance value with respect to the CCCD measurement, even if the current values (measured and imposed) were nearly the same. This is due to the aforementioned resistive component observed in the CV measurement that causes slight modification in the recorded shape with respect to the ideal rectangular one. Nonetheless, the quasi-solid device under study shows a very good capacity retention, under increased current density and scan rate.

The EDLC section was further tested in terms of long-term cycling performance, showing remarkable stability (see Fig. 3D), with an excellent capacitance retention (97% of the initial value) after 10 000 consecutive reversible cycles.

Finally, electrochemical impedance spectroscopy (EIS) analysis of the EDLC section was performed in 2-electrodes cell configuration with a $1 \times 2\ cm^2$ active surface (see Fig. 3E). A low equivalent series resistance of $21.8\ \Omega\ cm^2$ was found: if compared to the best literature reports on all solid state EDLCs [49,50], it testifies once more the high quality of the proposed polymer electrolyte.

Fig. 3F shows the current *vs.* potential profile of the DSSC device under 1 Sun irradiation. The photovoltaic efficiency (η) was evaluated as follows:

$$\eta = \frac{V_{OC}\, j_{SC}\, FF}{G} \tag{3}$$

where V_{OC} is the open circuit potential [V], j_{SC} is the short circuit current density [mA cm^{-2}], FF is the fill factor and G is the incoming electromagnetic radiation power [mW cm^{-2}] set to 100 mW cm^{-2}. The most important photovoltaic parameters are summarized in Table 1. η_C is the corrected photovoltaic efficiency (corrected with

Table 1
Photovoltaic parameters of the DSSC section in the integrated quasi-solid HS device.

η [%]	η_C [%]	V_{OC} [V]	j_{SC} [mA cm^{-2}]	V_{MP} [V]	j_{MP} [mA cm^{-2}]	FF [%]
2.60	4.33	0.63	11.96	0.43	6.05	34

respect to the effective active surface area of the Ti metal grid (0.6) support, which has an open area of 40% based on the material specifications); V_{MP} and j_{MP} are the potential and the current density at the maximum power point, respectively. A remarkable j_{SC} value was obtained (11.96 mA cm^{-2}), while the *FF* was quite low (34%) due to a somewhat high series resistance, which was already shown for this kind of DSSC based on quasi-solid electrolytes [31]. We may likely ascribe such a behaviour to a non-perfect electrode-electrolyte interfacial contact; nonetheless it does not negatively affect the overall response of the device, which shows excellent performance for a lab-scale truly quasi-solid system [51–53].

3.3. Characterization of the HS device

Harvesting-storage integration was investigated upon photo-charging and subsequent constant current discharge. The clamps of the source measure unit were connected to the electrodes of the HS device (EDLC side) to record the photo-charging potential. Fig. 4A shows the charging and discharging profiles. During photo-charge, the HS device was placed in the solar simulator, under 1 sun illumination condition (same test condition of the DSSC). The charge step was stopped to 0.55 V (even if the potential was slowly increasing), as for the obvious limiting plateau due to the V_{OC} of the DSSC. During discharge, light was switched off and the source measure unit was set in such a way as to apply a negative current. The integrated response was studied under various conditions by applying three different negative constant current densities. As expected, an increasing voltage drop was found at higher current values, in accordance to the CCCD in Fig. 4A.

The overall photo-electrical conversion and storage efficiency (OPECSE) was evaluated using the following equation:

$$OPECSE = \frac{\frac{1}{2} C V^2}{G t S} \quad (4)$$

where *C* is the capacitance of the EDLC (mF) evaluated from CCCD at the highest scan rate (0.35 A g^{-1}), *V* is the photo-charging potential (V), G is the electromagnetic radiation density provided by the sun simulator (mW cm^{-2}), *t* is the photo-charging time (s) and *S* is the active surface area of the DSSC (cm^2). For *C*, we selected the lowest capacitance value, evaluated at the highest current density during galvanostatic measurement. The OPECSE value represents the ratio between the energy stored into the EDLC section and the energy impinging onto the solar cell active surface. It is widely used in literature for evaluating the overall efficiency of integrated devices [1,32,33,54]. Since photo-charge is a dynamic process, which involves both photovoltaic and storage sections and their mutual electrical interaction, different OPECSE values were obtained as a function of time (see the OPECSE *vs.* time plot in Fig. 4B). The resulting scattered profile is comparable to the best recent literature reports [1,32,33]. A maximum of 3.72% was found in the very first seconds of charge and, afterwards, the OPECSE was found to decrease following an exponential trend. This is due to the potential saturation (plateau) that limits the energy stored in the EDLC, while the incoming electromagnetic energy keeps growing linearly with time, thus reducing the OPECSE value. In Fig. 4C, the OPECSE is also plotted as a function of the potential reached by the storage unit. This analysis, to our knowledge never shown before, is useful to assess precisely the best compromise between the final potential and the efficiency of any integrated device, which is fundamental in view of its practical application. It is worth noting that the OPECSE still mantains a high value of 3% at 0.45 V, which is close to the 0.55 V plateau reached during photocharge.

Table 2 provides a comparison of the newly developed integrated quasi-solid HS device under study, in terms of discharge current imposed after photocharge, recorded discharge capacity, PV efficiency and OPECSE value. In the last years, plenty of works were published in this field, and the use of different PV technologies accounts for huge differences in the obtained efficiencies. Thus, in Table 2 we listed data only for integrated HS devices based on DSSC or polymer solar cells (PSCs) harvesting units, to ensure proper direct comparison. Indeed, integrated devices based on perovskite

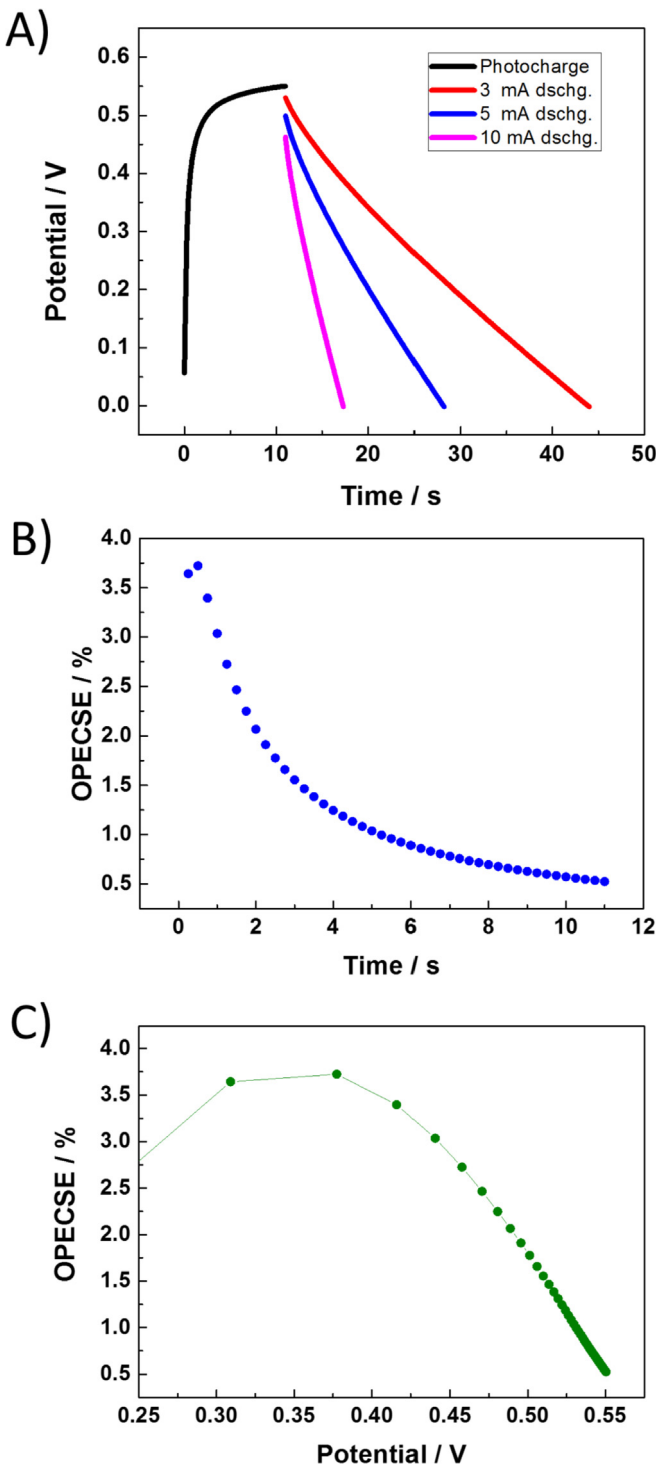

Fig. 4. Overall response of the integrated quasi-solid HS device. A) Photocharge and subsequent discharge curves, B) OPECSE values as a function of photo-charging time, C) OPECSE value as a function of the potential reached by the EDLC.

Table 2
Comparison of the performance of the newly developed integrated HS device under study with similar integrated HS devices reported in the literature, so far.

Reference	Discharge current [mA cm^{-2}]	Discharge capacity [mC cm^{-2}]	PV efficiency [%]	OPECSE [%]
This work	0.6	20	4.33	3.72
Chien et al. [43]	0.075	18	1.57	/[a]
Cohn et al. [44]	0.05	2.1	4.8	2.1
Xu et al. [33]	0.1	0.75	3.17	1.64
Yang et al. [45]	1.4	49	6.1	5.12

[a] The Authors did not calculate OPECSE values or calculated by different equation, thus direct comparison would be misleading.

solar cells recently demonstrated OPECSE values exceeding 10%. However, one should consider that these are based on liquid electrolytes (EDLC section) in most of the cases and, in particular, use a common three electrodes architecture.

Overall, normalized discharge capacity obtained in this work at 3 mA imposed discharge current, as well as OPECSE, are at the level of the best results reported so far in the literature; indeed, this is definitely remarkable considering that the scope of this work is demonstrating an innovative, simple and fashionable approach to fabricate 2-electrodes quasi-solid integrated HS architecture and not just push on a record performance with standard construction.

However, importantly, we used a higher discharge current density (0.6 mA cm^{-2}) with respect to most of the literature reports (except the work published by Yang et al. [45]). Thus, also the direct comparison of discharge capacity with Chien et al. [43], which appears as values comparable, is misleading. Indeed, using higher current ranges decreases EDLC capacity.

4. Conclusions

In summary, an innovative, smart, two-electrodes energy harvesting and storage device was proposed here, having an appreciably simplified architecture with respect to common literature reports. Indeed, DSSC and EDLC electrodes were hosted onto the same Ti metal grid, which effectively enabled the direct electronic path between harvesting and storage sections. This newly reported configuration was obtained exploiting a multifunctional polymer electrolyte platform, crosslinked by oxygen-inhibited UV-curing, and made of two poly(ethylene glycol)-based sections separated by a perfluorinated barrier, where one side is adapted to enable triiodide reduction in a dye-sensitized solar cell (DSSC), and the other side empowers on-board charge storage as an EDLC. A remarkable total device photo-electrical conversion and storage efficiency of 3.72% was obtained during photocharge under standard testing conditions (100 mW cm^{-2} and AM1.5G spectrum), which accounts for the remarkable characteristics of the novel multifunctional polymer-based platform. In addition, discharge curves subsequent to photo-charge were obtained with three different imposed currents, thus showing optimal performances under real operating conditions. This, along with the low cost and easy scalability of the different components, materials and manufacturing procedures, makes our newly proposed 2-electrodes integrated quasi-solid HS device a very promising candidate to intrude the next generation low power electronics market.

References

[1] Kim J, Lee SM, Hwang Y-H, Lee S, Park B, Jang J-H, et al. A highly efficient self-power pack system integrating supercapacitors and photovoltaics with an area-saving monolithic architecture. J Mater Chem A 2017;0:1–7. https://doi.org/10.1039/C6TA09117B.

[2] Guo W, Xue X, Wang S, Lin C, Wang ZL. An integrated power pack of dye-sensitized solar cell and Li battery based on double-sided TiO2 nanotube arrays. Nano Lett 2012;12:2520–3. https://doi.org/10.1021/nl3007159.

[3] Yang T, Xie D, Li Z, Zhu H. Recent advances in wearable tactile sensors: materials, sensing mechanisms, and device performance. Mater Sci Eng R Rep 2017;115:1–37. https://doi.org/10.1016/j.mser.2017.02.001.

[4] Volkov A, Gorbova E, Vylkov A, Medvedev D, Demin A, Tsiakaras P. Design and applications of potentiometric sensors based on proton-conducting ceramic materials. A brief review. Sensor Actuator B Chem 2017;244:1004–15. https://doi.org/10.1016/j.snb.2017.01.097.

[5] Chen S-L, Tao J, Tao H-J, Shen Y-Z, Wang T, Pan L. High-performance and low-cost dye-sensitized solar cells based on kesterite Cu2ZnSnS4 nanoplate arrays on a flexible carbon cloth cathode. J Power Sources 2016;330:28–36. https://doi.org/10.1016/j.jpowsour.2016.08.134.

[6] Zhang W, Zhu R, Li F, Wang Q, Liu B. High-performance solid-state organic dye sensitized solar cells with P3HT as hole transporter. J Phys Chem C 2011;115:7038–43. https://doi.org/10.1021/jp1118597.

[7] Zardetto V, Di Giacomo F, Garcia-Alonso D, Keuning W, Creatore M, Mazzuca C, et al. Fully plastic dye solar cell devices by low-temperature UV-irradiation of both the mesoporous TiO2 photo- and platinized counter-electrodes. Adv Energy Mater 2013;3:1292–8. https://doi.org/10.1002/aenm.201300101.

[8] Cheema H, Rodrigues RR, Delcamp JH. Sequential series multijunction dye-sensitized solar cells (SSM-DSCs): 4.7 volts from a single illuminated area. Energy Environ Sci 2017. https://doi.org/10.1039/C7EE01526G.

[9] Gurung A, Chen K, Khan R, Abdulkarim SS, Varnekar G, Pathak R, et al. Highly efficient perovskite solar cell photocharging of lithium ion battery using DC-DC booster. Adv Energy Mater 2017:1602105. https://doi.org/10.1002/aenm.201602105.

[10] Han Z, Zhao Z, Du Z, Zhao L, Cong X. A novel anode material of $TiCl_4$ treatment on Ag/TiO_2 in DSSC. Mater Lett 2014;136:424–6. https://doi.org/10.1016/j.matlet.2014.08.076.

[11] Du P, Hu X, Yi C, Liu HC, Liu P, Zhang HL, et al. Self-powered electronics by integration of flexible solid-state graphene-based supercapacitors with high performance perovskite hybrid solar cells. Adv Funct Mater 2015;25:2420–7. https://doi.org/10.1002/adfm.201500335.

[12] Xue X, Wang S, Guo W, Zhang Y, Wang ZL. Hybridizing energy conversion and storage in a mechanical-to- electrochemical process for self-charging power cell. Nano Lett 2012;12:5048–54. https://doi.org/10.1021/nl302879t.

[13] Ramadoss A, Saravanakumar B, Lee SW, Kim YS, Kim SJ, Wang ZL. Piezoelectric-driven self-charging supercapacitor power cell. ACS Nano 2015;9:4337–45. https://doi.org/10.1021/acsnano.5b00759.

[14] Chala S, Sengouga N, Yakuphanoğlu F, Rahmane S, Bdirina M, Karteri İ. Extraction of ZnO thin film parameters for modeling a ZnO/Si solar cell. Energy 2018;164. https://doi.org/10.1016/J.ENERGY.2018.09.035.

[15] Tehrani Z, Thomas DJ, Korochkina T, Phillips CO, Lupo D, Lehtim S, et al. Large-area printed supercapacitor technology for low-cost domestic green energy storage. Energy 2017;118. https://doi.org/10.1016/j.energy.2016.11.019.

[16] Ozan M, Akif E, Erkan Y, Sahmetlioglu E. Magnetic conductive polymer-graphene nanocomposites based supercapacitors for energy storage. Energy 2017;138:883–9. https://doi.org/10.1016/j.energy.2017.07.022.

[17] Bavio MA, Acosta GG, Kessler T, Visintin A. Flexible symmetric and asymmetric supercapacitors based in nanocomposites of carbon cloth/polyaniline - carbon nanotubes. Energy 2017;130:22–8. https://doi.org/10.1016/j.energy.2017.04.135.

[18] Rath T, Pramanik N, Kumar S. High electrochemical performance flexible solid-state supercapacitor based on Co-doped reduced graphene oxide and silk fi broin composites. Energy 2017;141:1982–8. https://doi.org/10.1016/j.energy.2017.11.126.

[19] Patil B, Ahn S, Park C, Song H, Jeong Y, Ahn H. Simple and novel strategy to fabricate ultra-thin , lightweight , stackable solid-state supercapacitors based on MnO 2 -incorporated CNT-web paper. Energy 2018;142:608–16. https://doi.org/10.1016/j.energy.2017.10.041.

[20] Iqbal MF, Ashiq MN, Hassan MU, Nawaz R, Masood A, Razaq A. Excellent electrochemical behavior of graphene oxide based aluminum sulfide nano-walls for supercapacitor applications. Energy 2018;159:151–9. https://doi.org/10.1016/j.energy.2018.06.123.

[21] Wang K, Gao F, Zhu Y, Liu H, Qi C, Yang K, et al. Internal resistance and heat generation of soft package Li4Ti5O12battery during charge and discharge. Energy 2018;149:364–73. https://doi.org/10.1016/j.energy.2018.02.052.

[22] Wang J, Li X, Zi Y, Wang S, Li Z, Zheng L, et al. A flexible fiber-based supercapacitor-triboelectric-nanogenerator power system for wearable electronics. Adv Mater 2015;27:4830–6. https://doi.org/10.1002/adma.201501934.

[23] Wang Q, Wang X, Xu J, Ouyang X, Hou X, Chen D, et al. Flexible coaxial-type fiber supercapacitor based on NiCo2O4 nanosheets electrodes. Nano Energy

2014;8:44–51. https://doi.org/10.1016/j.nanoen.2014.05.014.
[24] Cauda V, Stassi S, Lamberti A, Morello M, Fabrizio Pirri C, Canavese G. Leveraging ZnO morphologies in piezoelectric composites for mechanical energy harvesting. Nano Energy 2015;18:212–21. https://doi.org/10.1016/j.nanoen.2015.10.021.
[25] Maeng J, Meng C, Irazoqui PP. Wafer-scale integrated micro-supercapacitors on an ultrathin and highly flexible biomedical platform. Biomed Microdevices 2015;17. https://doi.org/10.1007/s10544-015-9930-4.
[26] Holmes CF. The role of lithium batteries in modern health care. J Power Sources 2001;97–98:739–41. https://doi.org/10.1016/S0378-7753(01)00601-2.
[27] Skunik-Nuckowska M, Grzejszczyk K, Kulesza PJ, Yang L, Vlachopoulos N, Häggman L, et al. Integration of solid-state dye-sensitized solar cell with metal oxide charge storage material into photoelectrochemical capacitor. J Power Sources 2013;234:91–9. https://doi.org/10.1016/j.jpowsour.2013.01.101.
[28] Liu R, Liu Y, Zou H, Song T, Sun B. Integrated solar capacitors for energy conversion and storage. Nano Res 2017;10:1–15. https://doi.org/10.1007/s12274-017-1450-5.
[29] Ng CH, Lim HN, Hayase S, Harrison I, Pandikumar A, Huang NM. Potential active materials for photo-supercapacitor: a review. J Power Sources 2015;296:169–85. https://doi.org/10.1016/j.jpowsour.2015.07.006.
[30] Chen HW, Hsu CY, Chen JG, Lee KM, Wang CC, Huang KC, et al. Plastic dye-sensitized photo-supercapacitor using electrophoretic deposition and compression methods. J Power Sources 2010;195:6225–31. https://doi.org/10.1016/j.jpowsour.2010.01.009.
[31] Scalia A, Bella F, Lamberti A, Bianco S, Gerbaldi C, Tresso E, et al. A flexible and portable powerpack by solid-state supercapacitor and dye-sensitized solar cell integration. J Power Sources 2017;359:311–21. https://doi.org/10.1016/j.jpowsour.2017.05.072.
[32] Xu J, Ku Z, Zhang Y, Chao D, Fan HJ. Integrated photo-supercapacitor based on PEDOT modified printable perovskite solar cell. Adv Mater Technol 2016:1–5. https://doi.org/10.1002/admt.201600074.
[33] Xu J, Wu H, Lu L, Leung S-F, Chen D, Chen X, et al. Supercapacitors: integrated photo-supercapacitor based on Bi-polar TiO $_2$ nanotube Arrays with selective one-side plasma-assisted hydrogenation (adv. Funct. Mater. 13/2014). Adv Funct Mater 2014;24. https://doi.org/10.1002/adfm.201470081. 1814–1814.
[34] Scalia A, Varzi A, Lamberti A, Tresso E, Jeong S, Jacob T, et al. High energy and high voltage integrated photo-electrochemical double layer capacitor. Sustain Energy Fuels 2018;2:968–77. https://doi.org/10.1039/C8SE00003D.
[35] Scalia A, Varzi A, Lamberti A, Jacob T, Passerini S. Portable high voltage powerpack by solid-state supercapacitor and dye-sensitized solar module integration. Front Chem 2018;6:443. https://doi.org/10.3389/FCHEM.2018.00443.
[36] Maiaugree W, Karaphun A, Pimsawad A, Amornkitbamrung V, Swatsitang E. Influence of SrTi1-xCoxO3NPs on electrocatalytic activity of SrTi1-xCoxO3NPs/PEDOT-PSS counter electrodes for high efficiency dye sensitized solar cells. Energy 2018;154:182–9. https://doi.org/10.1016/j.energy.2018.04.122.
[37] Arkan F, Izadyar M, Nakhaeipour A. The role of the electronic structure and solvent in the dye-sensitized solar cells based on Zn-porphyrins: theoretical study. Energy 2016;114:559–67. https://doi.org/10.1016/j.energy.2016.08.027.
[38] Alami AH, Rajab B, Aokal K. Assessment of silver nanowires infused with zinc oxide as a transparent electrode for dye-sensitized solar cell applications. Energy 2017;139:1231–6. https://doi.org/10.1016/j.energy.2017.03.171.
[39] Wongcharee K, Meeyoo V, Chavadej S. Dye-sensitized solar cell using natural dyes extracted from rosella and blue pea flowers. Sol Energy Mater Sol Cells 2007;91:566–71. https://doi.org/10.1016/j.solmat.2006.11.005.
[40] Jung HS, Lee JK. Dye sensitized solar cells for economically viable photovoltaic systems. J Phys Chem Lett 2013;4:1682–93. https://doi.org/10.1021/jz400112n.
[41] Gerosa M, Sacco A, Scalia A, Bella F, Chiodoni A, Quaglio M, et al. Toward totally flexible dye-sensitized solar cells based on titanium grids and polymeric electrolyte. IEEE J Photovoltaics 2016;6:498–505.
[42] Bella F, Pugliese D, Nair JR, Sacco A, Bianco S, Gerbaldi C, et al. A UV-cross-linked polymer electrolyte membrane for quasi-solid dye-sensitized solar cells with excellent efficiency and durability. Phys Chem Chem Phys 2013;15:3706–11. https://doi.org/10.1039/c3cp00059a.
[43] Chien CT, Hiralal P, Wang DY, Huang IS, Chen CC, Chen CW, et al. Graphene-based integrated photovoltaic energy harvesting/storage device. Small 2015;11:2929–37. https://doi.org/10.1002/smll.201403383.
[44] Cohn AP, Erwin WR, Share K, Oakes L, Westover AS, Carter RE, et al. All silicon electrode photocapacitor for integrated energy storage and conversion. Nano Lett 2015;15:2727–31. https://doi.org/10.1021/acs.nanolett.5b00563.
[45] Yang Z, Li L, Luo Y, He R, Qiu L, Lin H, et al. An integrated device for both photoelectric conversion and energy storage based on free-standing and aligned carbon nanotube film. J Mater Chem A 2013;1:954–8. https://doi.org/10.1039/C2TA00113F.
[46] Vitale A, Quaglio M, Chiodoni A, Bejtka K, Cocuzza M, Pirri CF, et al. Oxygen-inhibition lithography for the fabrication of multipolymeric structures. Adv Mater 2015;27:4560–5. https://doi.org/10.1002/adma.201501737.
[47] Jeong HE, Kwak R, Kim JK, Suh KY. Generation and self-replication of monolithic, dual-scale polymer structures by two-step capillary-force lithography. Small 2008;4:1913–8. https://doi.org/10.1002/smll.200800151.
[48] Zhang S, Pan N. Supercapacitors performance evaluation. Adv Energy Mater 2015;5:1–19. https://doi.org/10.1002/aenm.201401401.
[49] Ayalneh Tiruye G, Muñoz-Torrero D, Palma J, Anderson M, Marcilla R. All-solid state supercapacitors operating at 3.5 v by using ionic liquid based polymer electrolytes. J Power Sources 2015;279:472–80. https://doi.org/10.1016/j.jpowsour.2015.01.039.
[50] Tiruye GA, Muñoz-Torrero D, Palma J, Anderson M, Marcilla R. Performance of solid state supercapacitors based on polymer electrolytes containing different ionic liquids. J Power Sources 2016;326:560–8. https://doi.org/10.1016/j.jpowsour.2016.03.044.
[51] Mukhlish MZ Bin, Horie Y, Higashi K, Ichigi A, Guo S, Nomiyama T. Self-standing conductive ITO-silica nanofiber mats for use in flexible electronics and their application in dye-sensitized solar cells. Ceram Int 2017;43:8146–52. https://doi.org/10.1016/j.ceramint.2017.03.140.
[52] Song L, Yin X, Xie X, Du P, Xiong J, Ko F. Highly flexible TiO 2/C nanofibrous film for flexible dye-sensitized solar cells as a platinum- and transparent conducting oxide-free flexible counter electrode. Electrochim Acta 2017;255:256–65. https://doi.org/10.1016/j.electacta.2017.09.180.
[53] Saberi Motlagh M, Mottaghitalab V. The charge transport characterization of the polyaniline coated carbon fabric as a novel textile based counter electrode for flexible dye-sensitized solar cell. Electrochim Acta 2017;249:308–17. https://doi.org/10.1016/j.electacta.2017.08.032.
[54] Chen T, Qiu L, Yang Z, Cai Z, Ren J, Li H, et al. An integrated “energy wire” for both photoelectric conversion and energy storage. Angew Chem Int Ed 2012;51:11977–80. https://doi.org/10.1002/anie.201207023.